Activity-Based Imaging of Lipid Environments Targeted by Peroxynitrite in Biomimetic Vesicles and Live Cells

Bryan Gutierrez[1§], Tushar Aggarwal[1§], Huseyin Erguven[1], M. Rhia L. Stone[1], and Enver Cagri Izgu[1,2,3] *

(1) Department of Chemistry and Chemical Biology, Rutgers University, New Brunswick, NJ 08854, USA

(2) Cancer Institute of New Jersey, Rutgers University, New Brunswick, NJ 08901, USA

(3) Rutgers Center for Lipid Research, New Jersey Institute for Food, Nutrition, and Health, Rutgers University, New Brunswick, NJ 08901, USA

*Corresponding author: Izgu, E. C. (ec.izgu@rutgers.edu)
[§]These authors contributed equally

ABSTRACT

Lipid environments can be damaged by peroxynitrite ($ONOO^-$), a highly reactive redox species generated under nitrosative stress conditions. Strategies to investigate $ONOO^-$ via light microscopy are limited, and amphiphilic sensors capable of detecting $ONOO^-$ with high fidelity can make it possible to investigate peroxynitrite biochemistry at lipid environments. Here, we describe the development, characterization, and multifaceted utilization of a phospholipid-based probe, named **DPPC-TC-ONOO$^-$**, to directly visualize lipid environments targeted by $ONOO^-$ in both biomimetic and biological systems. Using **DPPC-TC-ONOO$^-$** and 1-palmitoyl-2-oleoyl-*sn*-glycero-3-phosphocholine, we built giant vesicles that can respond to $ONOO^-$ by lighting up at the membrane, with excellent selectivity against other redox species. We successfully delivered **DPPC-TC-ONOO$^-$** into live HeLa cells via lipid nanoparticles. Nitrosative stress led to enhanced fluorescence of the lipid clusters in the endoplasmic reticulum. This work offers an unprecedented chemical function for biomimetic protocell designs and reports a novel organelle-localized molecular probe to sense endogenous peroxynitrite in live cells.

INTRODUCTION

Lipids membranes mediate cellular growth, division, signal transduction, and waste disposal.[1–3] They compartmentalize the cell and its organelles and form tubular networks with substantial surface area. Lipid membranes regulate the location and activity of many membrane proteins.[3] These lipid-rich environments are potential targets of reactive nitrogen and oxygens species (RNS and ROS).[4,5]

Research geared toward membrane damage has garnered considerable attention with the discovery of ferroptosis, a non-apoptotic cell death mechanism characterized by iron-dependent accumulation of lipid peroxides.[6,7] Another major source of membrane damage is peroxynitrite ($ONOO^-$),[8] which is an aggressive RNS produced through the reaction between nitric oxide ($NO^•$) and superoxide ($O_2^{•-}$) at rates varying from 0.1–1 μM/min to 100 μM/min.[9,10] Peroxynitrite can serve as a signaling molecule[11] and be taken up by cells through anion transporters.[12] The mechanism of peroxynitrite-mediated lipid damage has been proposed to involve hydrogen-abstraction from unsaturated lipids, such as linolenic acid and arachidonic acid, generating carbon-centered lipid radicals[4,13] These radicals react with nearby unsaturated lipids and are trapped by molecular oxygen, forming lipid peroxides. Accumulation of these lipid peroxides and their lipid/protein degradation products have been linked to protein aggregation in neurons associated with Parkinson's disease.[14–16] Furthermore, peroxynitrite-induced lipid oxidation has been linked to the progression of cardiovascular diseases like diabetic cardiomyopathy.[17]

As peroxynitrite is emerging to be a key reactive species involved in cellular stress and different forms of pathophysiologies,[8,18,19] developing molecular tools to investigate its impact on lipids and subcellular environments of lipid assemblies has become increasingly important. Although there is a significant and evolving interest in developing bioimaging tools to study lipid membranes,[20–25] technologies for investigating peroxynitrite reactivity in lipid environments remain underdeveloped.[26,27]

Herein, we report the design, characterization, and multifaceted application of **DPPC-TC-ONOO$^-$**, a peroxynitrite probe derived from 1,2-dipalmitoyl-*rac*-glycero-3-phosphocholine (*rac*-DPPC). This phospholipid-based probe can localize in lipid membranes and directly sense proximal $ONOO^-$ in both biomimetic systems and live cells. Using **DPPC-TC-ONOO$^-$** and 1-palmitoyl-2-oleoyl-*sn*-glycero-3-phosphocholine (POPC), we built synthetic mimics of protocell membranes in the form of giant vesicles (GVs). These GVs responded to $ONOO^-$ by lighting up at the membrane, with the vesicle structures remaining intact. Additionally, they displayed excellent selectivity against other redox species, opening up new design opportunities for synthetic protocell architectures. We then utilized **DPPC-TC-ONOO$^-$** in live HeLa cells and demonstrated its localization in the endoplasmic reticulum. Nitrosative stress, induced through endogenous stimulation with interferon-γ (IFN-γ)/lipopolysaccharide (LPS)/phorbol myristate acetate (PMA) led to enhanced fluorescence of lipid clusters in the ER. This study offers a new molecular

tool to develop lipid-based self-assemblies capable of selectively sensing a chemical cue. In addition, **DPPC-TC-ONOO⁻** is a noninvasive tool that enables direct imaging of ONOO⁻ reactivity in live mammalian cells under nitrosative stress at the subcellular level.

RESULTS AND DISCUSSION

The peroxynitrite-sensing phospholipid and its non-amphiphilic analog were constructed through a modular chemical design. We developed a concise synthetic route for the peroxynitrite-sensing phospholipid, **DPPC-TC-ONOO⁻** (Scheme 1), which include a *p*-(4,4,4-trifluoro-3-oxobutyl)phenyl group as the peroxynitrite-reactive module,[28] 3-triazole-coumarin as the fluorophore, and the 1,2-dipalmitoyl-*rac*-glycero-3-phosphocholine (*rac*-DPPC) as the amphiphilic framework. In addition, to facilitate investigations of the peroxynitrite-mediated florescence activation mechanism and fidelity, we synthesized the non-amphiphilic analog **TEG-TC-ONOO⁻**, which contains a triethylene glycol (TEG) in place of *rac*-DPPC (Scheme 1). **TEG-TC-ONOO⁻** exists in a non-aggregated state in aqueous media, making the spectroscopic and spectrophotometric analyses of its redox reactions feasible. For both **DPPC-TC-ONOO⁻** and **TEG-TC-ONOO⁻**, the *p*-(4,4,4-trifluoro-3-oxobutyl)phenyl and 3-triazole-7- hydroxycoumarin groups were connected through a carbonate linkage. We reasoned that the carbonate linkage could mask 7-*O* of the coumarin, diminishing its fluorescence intensity. In the presence of ONOO⁻, the *p*-(4,4,4-trifluoro-

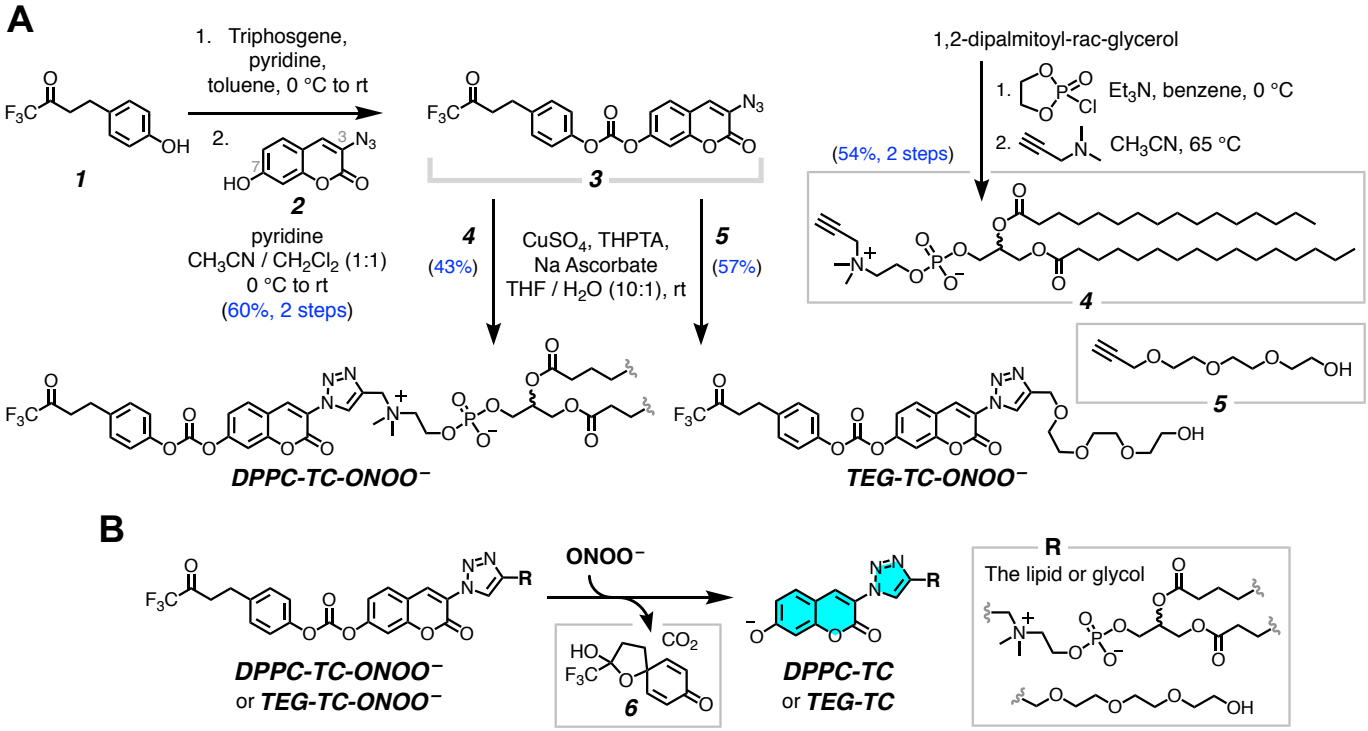

Scheme 1. (A) The chemical synthesis of **TEG-TC-ONOO⁻** and **DPPC-TC-ONOO⁻**. THPTA: tris(3-hydroxypropyltriazolyl-methyl)amine. **(B)** Peroxynitrite-mediated fluorescence activation of **TEG-TC-ONOO⁻** and **DPPC-TC-ONOO⁻**.

3-oxobutyl)phenyl moiety would undergo an oxidative elimination cascade, resulting in decarboxylative uncaging of the coumarin motif.

Both **DPPC-TC-ONOO$^-$** and **TEG-TC-ONOO$^-$** were synthesized through convergent routes in which the longest linear sequence required three chemical steps. First, 1,1,1-trifluoro-4-(4-hydroxyphenyl)butan-2-one (**1**) was converted to its chloroformate using triphosgene and successively connected with 3-azido-7-hydroxycoumarin (**2**) to furnish the carbonate **3** in 60% isolated yield over two steps. This peroxynitrite-sensitive compound served as a common intermediate in the construction of **DPPC-TC-ONOO$^-$** and **TEG-TC-ONOO$^-$**: Through the copper-catalyzed azide alkyne cycloaddition reaction, the carbonate **3** was conjugated with either the propargylated *rac*-DPPC **4** or propargyl-TEG-OH **5** to afford **DPPC-TC-ONOO$^-$** (43%) or **TEG-TC-ONOO$^-$** (57%), respectively. To obtain **4**, we converted 1,2-dipalmitoyl-*rac*-glycerol to its cyclic phosphate triester using ethylene chlorophosphite and opened the subsequent ring by the nucleophilic addition of 3-dimethylamino-1-propyne (see Supplementary Information for details).

Sensing occurs via oxidative uncaging of the coumarin motif and is specific to peroxynitrite. To gain a mechanistic insight into the reaction of the probes with ONOO$^-$, we conducted by liquid chromatography followed by high-resolution mass spectroscopy (LC-HRMS) (Figure S1). The amphiphilic probe, **DPPC-TC-ONOO$^-$**, displayed poor electrospray ionization profile, while **TEG-TC-ONOO$^-$** provided evidence for the formation of its oxidative decarboxylation product, **TEG-TC** upon mixing with ONOO$^-$. Further, we observed the progressive formation of the oxa-spiro[4,5] decenone **6**, supporting the proposed oxidative elimination process (cf. Scheme 1B).

We determined the pK_a of **TEG-TC** to be 7.1 ± 0.1 using UV-Vis spectrophotometric measurements (Figure S2). Under our confocal imaging conditions (pH 7.5–8.5 with cell-free assays, pH 7.4 with cells), a substantial population of the 7-hydroxycoumarin should exist in its aryloxide form. We assessed the change in coumarin fluorogenicity upon uncaging the probes from the oxobutylphenyl carbonate by measuring the relative fluorescence quantum yield ($\Phi_{F\mathit{rel}}$) values (Table 1) (see Supplementary Information for details). As the standard, we used coumarin 343, whose absolute fluorescence quantum yield (Φ_F) is 0.63 in ethanol.[29] The $\Phi_{F\mathit{rel}}$ values of **TEG-TC-ONOO$^-$** (entry 1) and **DPPC-TC-ONOO$^-$** (entry 3) were measured as 0.08 and 0.09, respectively. Each with a relatively low $\Phi_{F\mathit{rel}}$ and molar extinction coefficient, the probes were validated to exhibit weak brightness as a consequence of their coumarin 7-*O*-atom being derivatized as the carbonate. The $\Phi_{F\mathit{rel}}$ values for **TEG-TC** (entry 2) and **DPPC-TC** (entry 4), which were synthesized independently (see Supplementary Information for details), were measured as 0.66 and 0.64, respectively. Taken together, these results suggested that conversion of the caged coumarins to their uncaging products enhances the fluorescence quantum yield by ≥7-fold and brightness by ~30-fold.

Table 1. Characterization of the peroxynitrite probes and their uncaged forms.

Entry	Compound	Max Ex (nm)	Max Em (nm)	Extinction Coefficient (M^{-1} cm^{-1})	Quantum Yield	Brightness	Relative Brightness
1	**TEG-TC-ONOO⁻**	400.0	472.0	4475	0.08	358	1.4
2	**TEG-TC**	397.0	471.4	15613	0.66	10305	41.1
3	**DPPC-TC-ONOO⁻**	395.0	471.2	2784	0.09	251	1.0
4	**DPPC-TC**	398.0	472.0	13749	0.64	8799	35.1

The response rate and magnitude of **TEG-TC-ONOO⁻** against $ONOO^-$ was evaluated by measuring the relative fluorescence intensities of samples containing **TEG-TC-ONOO⁻** and **TEG-TC** (positive control) at 405 nm excitation (Figure 1A). These samples, prepared in Tris buffer (50 mM, pH 7.5), were measured over 60 minutes of incubation with and without $ONOO^-$. Physiologically normal $ONOO^-$ production rate in cells has been estimated to be in the single-digit μM range, while reaching up to 100 μM under dysregulated conditions.[8,30] Guided by this information, and in agreement with the fluorescence titration conditions employed for cytosolic resorufin-based peroxynitrite sensors,[31] we reasoned that administering 600 μM of $ONOO^-$ into a pH 7.5 medium would provide a steady level of effective $ONOO^-$ within a biologically relevant concentration range of ~10–20 μM/min. Upon addition of $ONOO^-$ (600 μM), the sample containing **TEG-TC-ONOO⁻** exhibited a rapid increase in fluorescence, reaching ~3-fold higher fluorescence within the first 10 minutes compared to the sample untreated. The difference in fluorescence

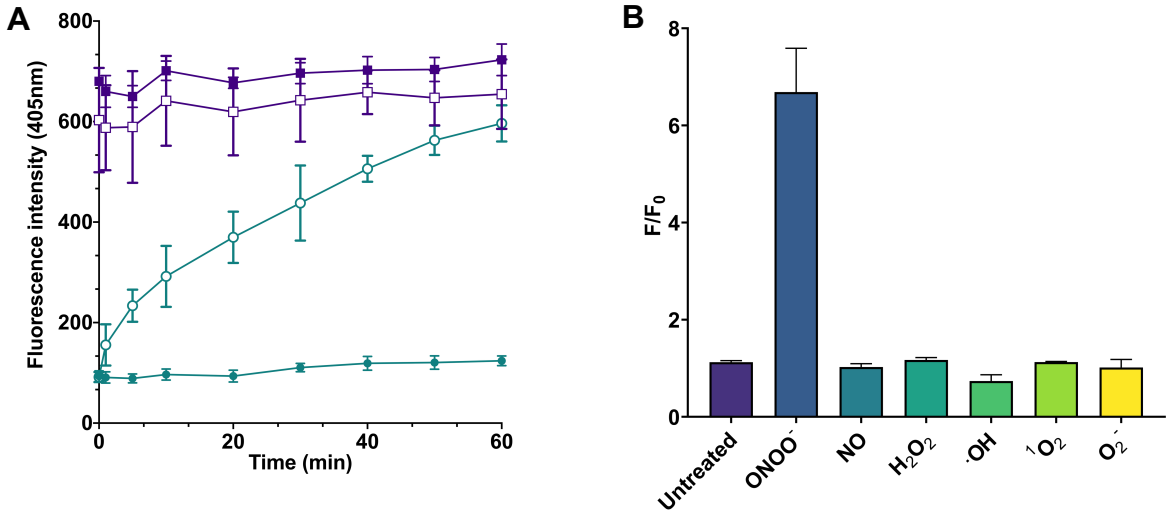

Figure 1. A. The time-dependent change in relative fluorescence intensities for probe **TEG-TC-ONOO⁻** (1 μM) and compound **TEG-TC** (1 μM) in Tris (50 mM, pH 7.5) upon addition of $ONOO^-$ (600 μM). Filled square: **TEG-TC**, hollow square: **TEG-TC** + $ONOO^-$, filled circle: **TEG-TC-ONOO⁻**, and hollow circle: **TEG-TC-ONOO⁻** + $ONOO^-$. Error bars represent standard deviation, $n = 3$. **B.** Relative fluorescence intensity (F) with respect to the background fluorescence intensity (F_0) of **TEG-TC-ONOO⁻** in the absence or presence of redox species. Probe **TEG-TC-ONOO⁻** (1 μM) was dissolved in Tris buffer (50 mM, pH 7.5) and subjected to RNS and ROS (600 μM): $ONOO^-$, $NO^\bullet$, H_2O_2, $HO^\bullet$, $^1O_2$, and $O_2^{\bullet-}$. Data represent F/F_0 measurements for samples incubated for 60 min. Plate reader was set to excitation at 405 nm and emission at 475 nm. Error bars represent standard deviation, $n = 3$.

between the peroxynitrite-treated and untreated samples reached up to 5-fold at the end of 60 minutes. During this time period, the relative fluorescence intensity of the sample containing **TEG-TC-ONOO**$^-$ became ~85% of that of the sample containing **TEG-TC** (positive control). This trend of increasing fluorescence output was mirrored in the level of conversion of **TEG-TC-ONOO**$^-$ into **TEG-TC** based on UV-Vis spectrophotometric measurements (Figure S3).

The peroxynitrite-specificity of the probe design was assessed by subjecting **TEG-TC-ONOO**$^-$ to other redox species, including $NO^\bullet$, hydrogen peroxide (H_2O_2), singlet oxygen ($^1O_2$), hydroxyl radicals ($HO^\bullet$), and $O_2^{\bullet-}$ (Figure 1B). Change in fluorescence intensity following excitation at 405 nm was measured over 60 minutes of incubation of **TEG-TC-ONOO**$^-$ with each species and presented based on the signal-to-background ratio F/F_0, where F and F_0 are defined as the fluorescence with and without the analyte. In the absence of a redox species, F/F_0 for **TEG-TC-ONOO**$^-$ increased only 13% (F/F_0 = 1.13) over 60 minutes. Treatment of **TEG-TC-ONOO**$^-$ with $ONOO^-$ gave rise to ~570% increase in fluorescence (F/F_0 = 6.69). Notably, incubating **TEG-TC-ONOO**$^-$ with species other than $ONOO^-$ resulted in only negligible levels of change in fluorescence. $NO^\bullet$, a free radical RNS that serves as a signaling molecule in cells, had essentially no effect on fluorescence intensity (F/F_0 = 1.03). The most significant fluorescence enhancement was observed for H_2O_2, with a fluorescence intensity 16% stronger than thatof the background (F/F_0 = 1.16). These results indicate that the relative fluorescence enhancement of **TEG-TC-ONOO**$^-$ is nearly 36-fold for $ONOO^-$ compared to the other RNS and ROS tested in this study.

Giant vesicles respond to peroxynitrite by lighting up at the membrane. In most biomimetic systems that rely on compartmentalization,[32] physical membrane boundaries are comprised of self-assembled lipids.[33] Biomimetic membranes can be represented by giant unilamellar vesicles (GUVs), which have dimensional properties (1–30 μm in diameter) relevant to those of mammalian cells (10–100 μm), display physical characteristics feasible for confocal fluorescence imaging, and are utilized for bottom-up construction of biomimetic systems.[34–36] We studied the membrane localization and chemical reactivity of **DPPC-TC-ONOO**$^-$ in GVs of mixed unilamellar and multilamellar populations (Figure 3A). Given the longer timescale required for data acquisition in microscopy compared to fluorescence measurements by plate reader, we set the pH of imaging buffers to 8.5, which extended the lifetime of peroxynitrite (Figure S4). We produced GVs from POPC and **DPPC-TC-ONOO**$^-$ (~99:1 molar ratio) using electroformation[37] (Figure S5). To label vesicle membranes, we employed 1,2-dioleoyl-*sn*-glycero-3-phosphoethanolamine-*N*-(lissamine rhodamine B sulfonyl) (18:1 Liss-Rhod PE) in 0.05 mol percent of the total lipid composition. Sucrose solution (400 mM) was used to hydrate the lipid films. A high solute concentration of sucrose facilitated the formation and stabilization of GV. Following electroformation, solutions of GVs were used within 24 hours. Vesicle size distribution was analyzed by dynamic light scattering (DLS), confirming the

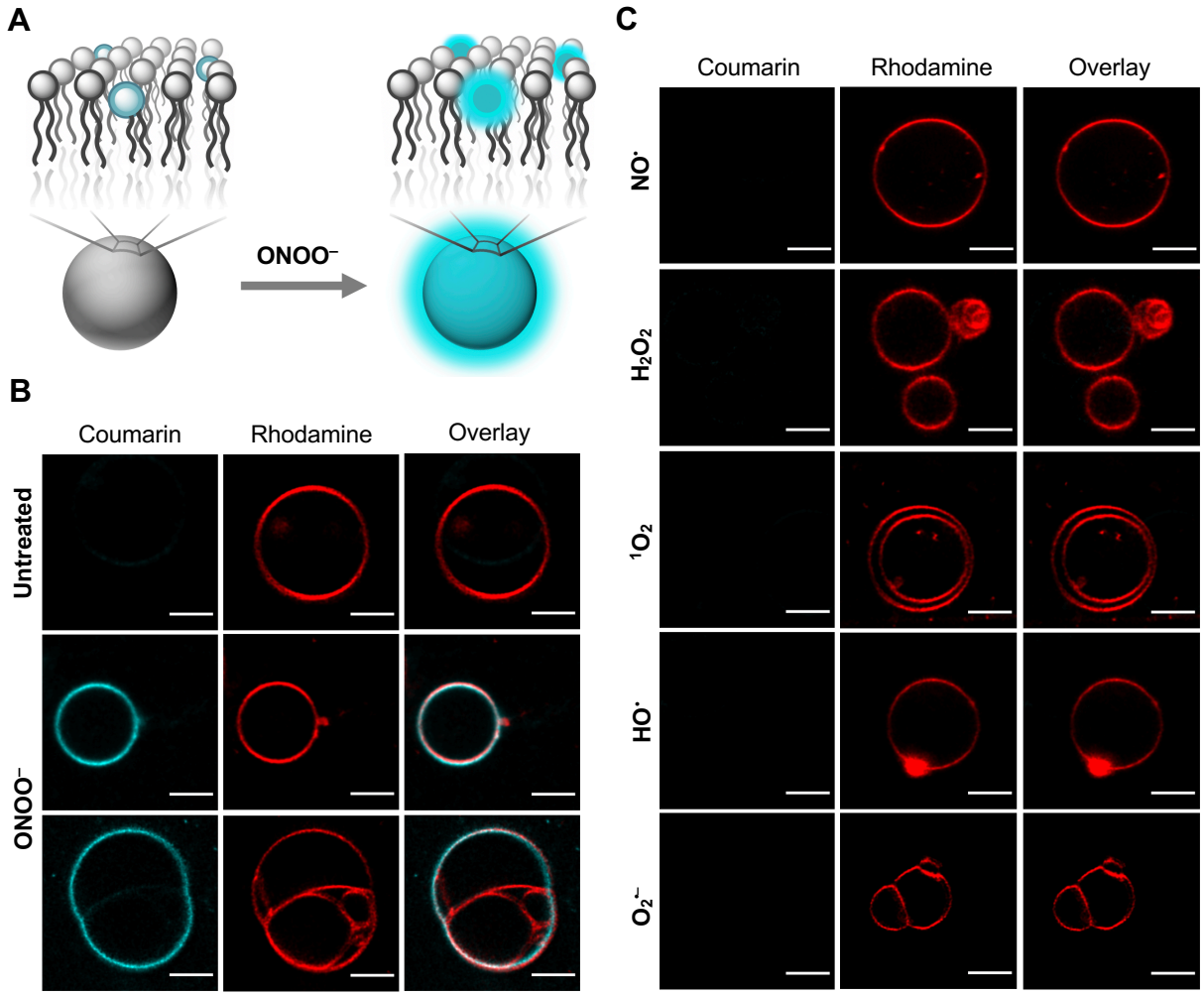

Figure 2. A. Functional protocell models that sense peroxynitrite. **B.** Confocal images acquired for untreated (top panel) and peroxynitrite-treated (middle and bottom panels) giant vesicles (GVs). **C.** Confocal images acquired for GVs treated with other RNS and ROS. **B-C.** Vesicles were prepared from POPC (98.5%, molar ratio) and **DPPC-TC-ONOO⁻** (1%) via electroformation. Liss-Rhod PE dye (red, 560 nm excitation) was used to label vesicle membranes. This dye, which constituted 0.5% of the lipid composition, was not displayed in panel **A** for simplicity. In the absence of peroxynitrite or in the presence of other RNS or ROS (100 μM), vesicles emit minimal fluorescence at the coumarin channel (405 nm excitation). Vesicles are activated to emit strong fluorescence when peroxynitrite (100 μM) is present. Fluorescence images (coumarin, rhodamine, and a merge of both channels) are shown for each field of view to demonstrate the localization of the fluorescent phospholipid **DPPC-TC***, generated by peroxynitrite *in-situ*, with respect to the vesicle membranes. Scale bar = 5 μm.

presence of GVs. DLS analysis showed that 91% of vesicles had diameters ranging from ~5 to 20 μm, with 48% had an average size of 5 μm in diameter (Figure S6). GVs were then imaged using fluorescence confocal microscopy. The vesicles were treated with the redox species, then mounted directly onto a microscope slide. Although significant vesicle motility was observed, the population density was sufficiently high to locate some static vesicles. Addition of $ONOO^-$ (100 μM final concentration) into mixture of GVs led to a substantial increase in membrane fluorescence at 405 nm excitation (Figure 3B), which was consistent with the observations of **TEG-TC-ONOO⁻** in the vesicle-free assays (Figure 1B). Notably,

DPPC-TC-ONOO$^-$ makes the redox-sensing function of GVs highly selective towards $ONOO^-$. Incubation (5 min) with other redox species, including $NO^\bullet$, H_2O_2, $HO^\bullet$, $^1O_2$, and $O_2^{\bullet-}$, resulted in essentially no fluorescence generation following excitation at 405 nm (Figure 2C). Taken together, these results indicate that **DPPC-TC-ONOO$^-$** i) can localize into the vesicle membranes made of POPC, a natural phospholipid, ii) induces no biophysical alteration to the membrane upon being activated by $ONOO^-$, and iii) detection of $ONOO^-$ can be achieved with high redox selectivity.

DPPC-TC-ONOO$^-$ allows direct imaging of intracellular lipid environments targeted by peroxynitrite. With the utility of **DPPC-TC-ONOO$^-$** proven in synthetic protocell membranes, we sought to incorporate it into live HeLa cells, which are relevant to redox-induced stress and have well-recognized pathways for RNS and ROS production. Although a standard liposome formation method was initially attempted, significant optimization of buffer and lipid concentration was performed in order to circumvent the limited solubility of **DPPC-TC-ONOO$^-$**. This can be rationalized by considering that the parent DPPC headgroup is modified with the relatively hydrophobic butanone-coumarin motif, possibly decreasing the overall polarity of the molecule. Therefore, we utilized lipid nanoparticles (LNPs) (~100 nm in diameter) to deliver **DPPC-TC-ONOO$^-$**. LNPs were obtained via sonication from 1,2-di-*O*-octadecenyl-3-trimethylammonium propane (DOTMA), 1,2-dioleoyl-*sn*-glycero-3-phosphoethanolamine (DOPE), and **DPPC-TC-ONOO$^-$** (47.5 : 47.5 : 5.0 molar ratio), which were hydrated with a 300 mM sucrose solution. DOTMA and DOPE were chosen as the carrier lipids due to their cationic/zwitterionic natures, which has been postulated to enhance attraction to the negatively charged cell membrane.[38] Sucrose proved to be the ideal medium in comparison to PBS, cell-compatible medium (Hanks' Balanced Salt Solution, HBSS), and Dulbecco's Modified Eagle Medium (DMEM). Lipid vesicles are stable in sucrose as demonstrated above, and at 300 mM concentration sucrose possess the same osmolarity as cell media[39], making it a suitable medium to handle LNPs.

The impact of different LNP compositions and incubation times on the cellular incorporation of **DPPC-TC-ONOO$^-$** was assessed. LNPs prepared in HBSS were added to live HeLa cells, which were then imaged by confocal microscopy. Initial trials indicated that the molar concentration of **DPPC-TC-ONOO$^-$** in LNPs influenced both the homogeneity of the LNPs and the fluorescence signal generation within stimulated cells. Specifically, LNPs containing greater than 10 mol% **DPPC-TC-ONOO$^-$** were considerably more heterogenous in size (up to 20 μm observed, in contrast to ~100 nm) and nonuniform in vesicle lamellarity. In contrast, less than 4 mol% **DPPC-TC-ONOO$^-$** generated insufficient fluorescence signal upon probe uncaging. To balance these counteracting factors, 5% **DPPC-TC-ONOO$^-$** was used, with 47.5% DOTMA and DOPE, each. Also in these initial assays, cells were incubated with LNPs for up to 15 hours to complete the uptake and subcellular localization of **DPPC-TC-ONOO$^-$**. Shorter incubation times

(~3–5 hours) led to cellular uptake but not localization. To accommodate extended incubation timeframes, LNPs were prepared in cell medium (DMEM) instead of HBSS, which we observed to be deleterious to the cells for incubations exceeding 3 hours. However, high serum concentration in DMEM caused interference between LNPs and serum-protein, resulting in aggregate formation as observed by microscopy. To overcome this obstacle, we used LNPs (50 μM) prepared in a mixture of 2/3 volumetric ratio of sucrose solution and Opti-MEM™, a reduced serum medium known to increase the efficiency of lipofection.[40]

With a feasible liposome preparation and treatment protocol established for live HeLa cell imaging, we then turned attention to assessing the cytocompatibility of the LNPs, with or without **DPPC-TC-ONOO$^-$**, **DPPC-TC**, and the oxa-spiro[4,5] decenone **6**. We employed a standard 3-(4,5-dimethylthiazol-2-yl)-2,5-diphenyl tetrazolium bromide (MTT) cell viability assay in HeLa cells treated with these molecules (8–250 μM) over a 24-hour period. The dose-response curves (Figure S7) provided high IC_{50} values (>100 μM) for each (Table S1), suggesting that LNPs (50 μM) and the byproducts of the peroxynitrite reaction exhibit insignificant levels of cytotoxicity under our cell imaging conditions.

The utility of **DPPC-TC-ONOO$^-$** was demonstrated in live HeLa cell imaging (Figure 3). For a physiologically relevant nitrosative stress model, we employed the standard stimulation condition involving IFN-γ/LPS/PMA. Treatment of cells with IFN-γ/LPS leads to the endogenous production of nitric oxide and PMA provokes increased levels of superoxide.[41] These two reactive species combine to form peroxynitrite, as described above. HeLa cells treated with LNPs containing **DPPC-TC** (positive control) exhibited strong coumarin fluorescence at 405/475 nm (presented here as DPPC-TC channel) (Figure 3A). In contrast, those treated with LNPs containing **DPPC-TC-ONOO$^-$** and left unstimulated (negative control) generated no observable signal (Figure 3B). Upon endogenous peroxynitrite generation through stimulation with IFN-γ/LPS/PMA, we observed a substantial increase in fluorescence at 405/475 nm (Figures 3C, 3F-I). The signal brightness of these stimulated cells after 60 minutes of incubation were comparable to that of the positive control. Notably, upon PMA addition following the IFN-γ/LPS stimulation, the intracellular fluorescence was observable at the 3-minute time point (the earliest possible image acquisition time after cell treatment in our imaging setup), indicating that PMA instantly leads to $ONOO^-$ production and that **DPPC-TC-ONOO$^-$** can rapidly sense proximal $ONOO^-$. The change in signal intensity after 30 minutes was negligible, suggesting the possibility of probe consumption and/or lack of proximal peroxynitrite. We also evaluated the intracellular redox selectivity of **DPPC-TC-ONOO$^-$** using *N*-(3-(aminomethyl)benzyl)-acetamidine, known as 1400W, which inhibits the production of $NO^{\bullet}$ by irreversibly binding to iNOS.[42] The cells treated with 1400W only (Figure 3D) or treated with 1400W and IFN-γ/LPS/PMA (Figure 3E) generated no observable signal in the DPPC-TC channel. These controls showed that **DPPC-TC-ONOO$^-$** selectively senses peroxynitrite generated from iNOS in response to nitrosative but not oxidative stress.

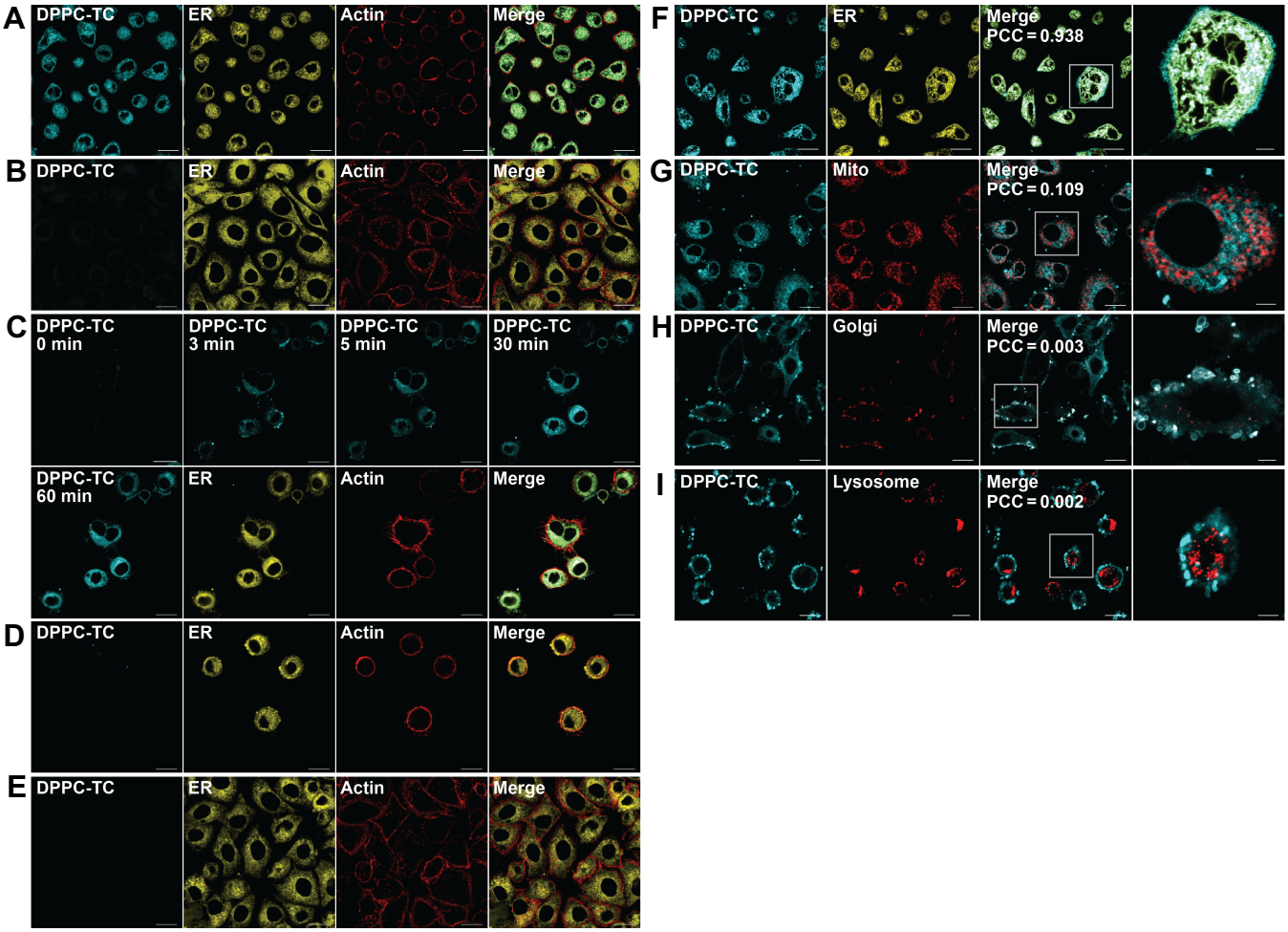

Figure 3. Confocal imaging of lipid environments targeted by ONOO⁻ in live HeLa. Cells were seeded into glass microscope dishes, incubated with LNPs (50 μM) and stained with organelle trackers and/or actin dye prior to imaging. LNPs obtained from a 47.5: 47.5:5.0 molar ratio of DOTMA, DOPE, and **(A) DPPC-TC** or **(B–I) DPPC-TC-ONOO⁻**. **(A-B)** Cells treated with LNPs, left unstimulated. **(C)** Cells treated with LNPs, stimulated with IFN-γ/LPS/PMA. Time coarse images acquired upon PMA treatment. **(D)** Cells treated with LNPs and 1400W. **(E)** Cells treated with LNPs, then with 1400W and IFN-γ/LPS/PMA. **(F-I)** Quantitative colocalization study of cells treated with LNPs and stimulated with IFN-γ/LPS/PMA. Pearson's correlation coefficient (PCC) was calculated for quantitative assessment of colocalization. Organelle trackers: ER-Tracker™, MitoTracker™, CellLight™ Golgi-RFP, LysoTracker™. Cell cytoskeleton was assessed with CellMask™ Deep Red Actin Tracking Stain. DPPC-TC channel: 405/475 nm. Scale bars = 20 μm or 5 μm (zoomed area).

To determine whether **DPPC-TC-ONOO⁻** localizes and functions at a specific subcellular compartment in HeLa, we carried out a comprehensive colocalization study with dyes specific for lipid-rich and membrane-enclosed organelles, including the ER, mitochondrion, Golgi apparatus, and lysosome (Figures 3F-I). In addition, we used actin stain to gain a visual insight into the cytoskeletal structure of the whole cell. To assess the degree of colocalization quantitatively, we determined the Pearson's correlation coefficients (PCC) of the signal from **DPPC-TC** overlapping with that from the organelle tracker dyes. The

DPPC-TC signal merged almost perfectly (PCC = 0.938) with the perinuclear signal of ER-Tracker™ Green (Figure 3F), suggesting a high statistical correlation and preference of **DPPC-TC-ONOO⁻** to localize in the ER. Cells stained with dyes specific for mitochondria, Golgi, and lysosomes displayed poor statistical correlation (PCC ~ 0.1 or less) (Figures 3G-I).

CONCLUSION

The concentrations of reactive species and redox mechanisms are tightly controlled in order to maintain cell homeostasis and minimize side reactions causing cell damage.[8,43,44] In this work, we described the development and applications of a DPPC-derived probe **DPPC-TC-ONOO⁻** for imaging lipid environments targeted by peroxynitrite. Using this designer phospholipid and POPC, we built synthetic protocell membranes in the form of GVs. These GVs responded to $ONOO^-$ by lighting up at the membrane, remained physically intact, and showed excellent selectivity against other redox species. **DPPC-TC-ONOO⁻** was successfully incorporated into HeLa cells through cationic/zwitterionic lipid nanoparticles. Endogenously produced peroxynitrite, through the stimulation of cells with IFN-γ/LPS/PMA, resulted in significant enhancement in fluorescence at the subcellular level. Comprehensive colocalization studies indicated that **DPPC-TC-ONOO⁻** localizes primarily in the ER and the detection of peroxynitrite reactivity near the ER is rapid (≤3 minutes) upon PMA addition.

Interest in expanding the chemical toolbox of synthetic lipids is surging and demand for applying these tools in both basic research and biomedicine is substantial.[45–47] Our work opens a platform for the development of lipid self-assemblies capable of sensing a chemical cue, offering a new design opportunity for synthetic protocells[48–52] and a purely chemical perspective to cell-free biosensing.[53] In addition, **DPPC-TC-ONOO⁻** enables real-time investigation of the ER during cellular nitrosative stress. This ER-localized bioimaging tool can be leveraged to help untangle redox stress mechanisms that damage the eukaryotic cells. The ER, which functions in protein synthesis and folding,[54] must maintain its redox homeostasis to facilitate disulfide bridge formation in proteins,[55] and the ER membrane is a key site for lipid peroxidation in ferroptosis,[56] highlighting the importance of ER-specific redox probing.

SUPPLEMENTARY INFORMATION

The Supplementary Information includes chemicals, methods and characterization for syntheses; method details for vesicle preparations; spectrophotometric measurements; cell viability assay; and supplementary figures.

ACKNOWLEDGMENT

We thank Dr. Ki-Bum Lee for allowing access to the fluorescence plate reader and we acknowledge Meizi Chen and Liming Wang for their assistance with fluorescence assays.

FUNDING SOURCES

This work was supported by the US National Institutes of Health (NIH) / NIBIB Trailblazer Award (EB029548), the Rutgers Center for Lipid Research, the American Cancer Society, Institutional Research Grant Early Investigator Award, and the Rutgers Cancer Institute of New Jersey NCI Cancer Center Support Grant (P30CA072720).

AUTHOR CONTRIBUTIONS

E.C.I. conceived the study. B.G. and H.E. conducted the synthesis of the probes and spectroscopic and spectrophotometric analyses. B.G. established protocols for the preparation of giant vesicles. T.A. and M.R.L.S. prepared LNPs and performed the microscopy and cell work. T.A. performed the pK_a measurement and MTT assay. All of the authors contributed to the interpretation of data. E.C.I. wrote the manuscript with input from all authors. E.C.I. supervised the study.

DECLARATION OF INTEREST

The authors declare no competing interests.

REFERENCES

1. Harayama, T., Riezman, H. Understanding the diversity of membrane lipid composition. *Nat. Rev. Mol. Cell Biol.* (2018), *19*, 281–296.
2. Carlton, J. G., Jones, H., Eggert, U. S. Membrane and organelle dynamics during cell division. *Nat. Rev. Mol. Cell Biol.* (2020), *21*, 151–166.
3. Escriba, P. V., Gonzalez-Ros, J. M., Goni, F. M., Kinnunen, P. K. J., Vigh, L., Sanchez-Magraner, L., Fernandez, A. M., Busquets, X., Horvath, I., Barcelo-Coblijn, G. Membranes: a meeting point for lipids, proteins and therapies. *J. Cell. Mol. Med.* (2008), *12*, 829– 875.
4. Rubbo, H., Trostchansky, A., O'Donnell, V. Peroxynitrite-mediated lipid oxidation and nitration: mechanisms and consequences. *Arc. Biochem. Biophys.* (2009), *484*, 167–172.
5. Radi, R. Oxygen radicals, nitric oxide, and peroxynitrite: Redox pathways in molecular medicine. *Proc. Natl. Acad. Sci. U.S.A.* (2018), *115*, 5839–5848.
6. Dixon, Scott J., Lemberg, Kathryn M., Lamprecht, Michael R., Skouta, R., Zaitsev, Eleina M., Gleason, Caroline E., Patel, Darpan N., Bauer, Andras J., Cantley, Alexandra M., Yang, Wan S.,

Morrison, B., Stockwell, Brent R. Ferroptosis: an iron-dependent form of nonapoptotic cell death. *Cell* (2012), *149*, 1060–1072.

7. Stockwell, B. R., Friedmann Angeli, J. P., Bayir, H., Bush, A. I., Conrad, M., Dixon, S. J., Fulda, S., Gascón, S., Hatzios, S. K., Kagan, V. E., Noel, K., Jiang, X., Linkermann, A., Murphy, M. E., Overholtzer, M., Oyagi, A., Pagnussat, G. C., Park, J., Ran, Q., Rosenfeld, C. S., Salnikow, K., Tang, D., Torti, F. M., Torti, S. V., Toyokuni, S., Woerpel, K. A., Zhang, D. D. Ferroptosis: a regulated cell death nexus linking metabolism, redox biology, and disease. *Cell* (2017), *171*, 273–285.

8. Szabo, C.; Ischiropoulos, H.; Radi, R. Peroxynitrite: biochemistry, pathophysiology and development of therapeutics. *Nat. Rev. Drug Discov.* (2007), *6*, 662–680.

9. Radi, R., Peluffo, G., Alvarez, M. N., Naviliat, M., Cayota, A. Unraveling peroxynitrite formation in biological systems. *Free Radical Biol. Med.* (2001), *30*, 463–488.

10. Alvarez, M. N., Piacenza, L., Irigoin, F., Peluffo, G., Radi, R. Macrophage-derived peroxynitrite diffusion and toxicity to *Trypanosoma cruzi*. *Arch. Biochem. Biophys*. (2004), *432*, 222–232.

11. Liaudet, L.; Vassalli, G.; Pacher, P. Role of peroxynitrite in the redox regulation of cell signal transduction pathways. *Front Biosci (Landmark Ed).* (2009), *12*, 4809–4814.

12. Ferrer-Sueta, G.; Radi, R. Chemical biology of peroxynitrite: kinetics, diffusion, and radicals. *ACS Chem. Biol.* (2009), *4*, 161–177.

13. Squadrito, G.; Pryor, W. Oxidative chemistry of nitric oxide: the roles of superoxide, peroxynitrite, and carbon dioxide. *Free Radic. Biol. Med.* (1998), *25*, 392–403.

14. Perrin, R. J.; Woods, W. S.; Clayton, D. F.; George, J. M. Exposure to long chain polyunsaturated fatty acids triggers rapid multimerization of synucleins. *J. Biol. Chem*. (2001), *276*, 41958–41962.

15. Dawson, T. M.; Dawson, V. L. Molecular pathways of neurodegeneration in parkinson's disease. *Science* (2003), *302*, 819–822.

16. Vera, D.; Junn, E.; Mouradian, M. M. The role of oxidative stress in parkinson's disease. *J. Parkinson's Dis.* (2013), *3*, 461–491.

17. Pacher, P.; Schulz, R.; Liaudet, L.; Szabo, C. Nitrosative stress and pharmacological modulation of heart failure. *Trends Pharmacol. Sci.* (2005), *26*, 302–310.

18. Pacher, P.; Beckman, J. S.; Liaudet, L. Nitric oxide and peroxynitrite in health and disease. *Physiol. Rev.* (2007), *87*, 315–424.

19. Wang, F.; Yuan, Q.; Chen, F.; Pang, J.; Pan, C.; Xu, F.; Chen, Y. Fundamental mechanisms of the cell death caused by nitrosative stress. *Front. Cell Dev. Biol*. (2021)*, 9*, 1–9.

20. Klier, P. E. Z.; Gest, A. M. M.; Martin, J. G.; Roo, R.; Navarro, M. X.; Lesiak, L.; Deal, P. E.; Dadina, N.; Tyson, J.; Schepartz, A., Miller, E. W. Bioorthogonal, fluorogenic targeting of voltage-sensitive fluorophores for visualizing membrane potential dynamics in cellular organelles. *J. Am. Chem. Soc.* (2022), *144*, 12138–12146.

21. Danylchuk, D. I.; Jouard, P.-H.; Klymchenko, A. S. Targeted solvatochromic fluorescent probes for imaging lipid order in organelles under oxidative and mechanical stress. *J. Am. Chem. Soc.* (2021), *143*, 912–924.

22. Dadina. N.; Tyson, J.; Zheng, S.; Lesiak, L.; Schepartz, A. Imaging organelle membranes in live cells at the nanoscale with lipid-based fluorescent probes. *Curr. Opin. Chem. Biol.* (2021), *65*,154–162.

23. Aparin, I. O., Yan, R., Pelletier, R., Choi, A. A., Danylchuk, D. I., Xu, K., Klymchenko, A. S. Fluorogenic dimers as bright switchable probes for enhanced super-resolution imaging of cell membranes. *J. Am. Chem. Soc.* (2022), *144*, 18043–18053.

24. Klymchenko, A. S., Kreder, R. Fluorescent probes for lipid rafts: from model membranes to living cells. *Chem. Biol.* (2014), *21*, 97–113.

25. Klymchenko, A. S. Fluorescent probes for lipid membranes: from the cell surface to organelles. *Acc. Chem. Res.* (2023), *56*, 1–12.

26. Soh, N.; Makihara, K.; Ariyoshi, T.; Seto, D.; Maki, T.; Nakajima, H.; Nakano, K.; Imato, T. Phospholipid-linked coumarin: A fluorescent probe for sensing hydroxyl radicals in lipid membranes. *Anal. Sci.* (2008), *24*, 293– 296.

27. Knewtson, K. E.; Rane, D.; Peterson, B. R. Targeting fluorescent sensors to endoplasmic reticulum membranes enables detection of peroxynitrite during cellular phagocytosis. *ACS Chem. Biol.* (2018), *13*, 2595–2602.

28. Yang, D.; Wang, H.-L.; Sun, Z.-N.; Chung, N.-W.; Shen, J.-G., A highly selective fluorescent probe for the detection and imaging of peroxynitrite in living cells. *J. Am. Chem. Soc.* (2006), *128*, 6004–6005.

29. Reynolds, G.A.; Drexhage, K.H.; New coumarin dyes with rigidized structure for flashlamp-pumped dye lasers. *Optics Commun.* (1975), *13*, 222–225.

30. Carballal, S.; Bartesaghi, S.; Radi, R. Kinetic and mechanistic considerations to assess the biological fate of peroxynitrite. *Biochim. Biophys. Acta.* (2014), *1840*, 768–780.

31. Zhang, Q.; Zhu, Z.; Zheng, Y.; Cheng, J.; Zhang, N.; Long, Y. A three-channel fluorescent probe that distinguishes peroxynitrite from hypochlorite. *J. Am. Chem. Soc*. (2012), *134*, 18479–18482.

32. Cho, E.; Lu, Y. Compartmentalizing cell-free systems: Toward creating life-like artificial cells and beyond. *ACS Synth. Biol.* (2020), *9*, 2881–2901.

33. Sezgin, E.; Levental, L.; Mayor, S.; Eggeling C. The mystery of membrane organization: composition, regulation, and roles of lipid rafts. *Nat. Rev. Mol. Cell. Bio.* (2017), *18*, 361–374.

34. Kurihara, K.; Okura, Y.; Matsuo, M.; Toyota, T.; Suzuki, K.; Sugawara, T. A recursive vesicle-based model protocell with a primitive model cell cycle. *Nat. Commun.* (2015), *6*, 8352.

35. Weiss, M.; Frohnmayer, J. P.; Benk, L. T.; Haller, B.; Janiesch, J.- W.; Heitkamp, T.; Börsch, M.; Lira, R. B.; Dimova, R.; Lipowsky, R.; Bodenschatz, E.; Baret, J.- C.; Vidakovic-Koch, T.; Sundmacher, K.; Platzman, I.; Spatz, J. P. Sequential bottom-up assembly of mechanically stabilized synthetic cells by microfluidics. *Nat. Mater.* (2017), *17*, 89.

36. Göpfrich, K.; Haller, B.; Staufer, O.; Dreher, Y.; Mersdorf, U.; Platzman, I.; Spatz, J. P. One-pot assembly of complex giant unilamellar vesicle-based synthetic cells. *ACS Synth. Biol.* (2019), *8*, 937–947.

37. Stein, H.; Spindler, S.; Bonakdar, N.; Wang, C.; Sandoghdar, V. Production of isolated giant unilamellar vesicles under high salt concentrations. *Front. Physiol.* (2017), 8, 63.

38. Felgner, P. L.; Gadek, T. R.; Holm, M.; Roman, R.; Chan, H. W.; Wenz, M.; Northrop, J. P.; Ringold, G. M.; Danielsen, M. Lipofection: a highly efficient, lipid-mediated DNA-transfection procedure. *Proc. Natl. Acad. Sci. USA.* (1987), *21*, 7413–7417.

39. Waymouth, C. Osmolality of mammalian blood and of media for culture of mammalian cells. *In Vitro* (1970), *6*, 109–127.

40. Young, A. T.; Moore, R. B.; Murray, A. G.; Mullen, J. C.; Lakey, J. R. Assessment of different transfection parameters in efficiency optimization. *Cell Transplant.* (2004), *2*, 79–85.

41. Pfeiffer, S.; Lass, A.; Schmidt, K.; Mayer, B. Protein tyrosine nitration in cytokine-activated murine macrophages. *J. Biol. Chem.* (2001), *276*, 34051–34058.

42. Garvey, E. P., Oplinger, J. A., Furfine, E. S., Kiff, R. J., Laszlo, F., Whittle, B. J., Knowles, R. G. 1400W is a slow, tight binding, and highly selective inhibitor of inducible nitric-oxide synthase in vitro and in vivo. *J. Biol. Chem*. (1997), *272*, 4959–4963.

43. Jiang, X.; Stockwell, B. R.; Conrad, M. Ferroptosis: mechanisms, biology and role in disease. *Nat. Rev. Mol. Cell Biol.* (2021), *22*, 266–282.

44. Cheung, E. C.; Vousden, K. H. The role of ROS in tumour development and progression. *Nat. Rev. Cancer.* (2022), 5, 280–297.

45. Klymchenko, A. S.; Kreder, R. Fluorescent probes for lipid rafts: From model membranes to living cells. *Chem. Biol.* (2014), *21*, 97–113.

46. Flores, J.; White, B. M.; Brea, R. J.; Baskin, J. M.; Devaraj, N. K. Lipids: chemical tools for their synthesis, modification, and analysis. *Chem. Soc. Rev.* (2020), *49*, 4602–4614.

47. Mukhopadhyay, T. K.; Morstein, J.; Trauner, D., Photopharmacological control of cell signaling with photoswitchable lipids. *Curr. Opin. Pharmacol.* (2022), *63*, 102202.

48. Viricel, W.; Mbarek, A.; Leblond, J. Switchable lipids: Conformational change for fast pH-triggered cytoplasmic delivery. *Angew. Chem. Int. Ed.* (2015), *54*, 12743–12747.

49. Kamat, N. P.; Tobe, S.; Hill, I. T.; Szostak, J. W. Electrostatic localization of RNA to protocell membranes by cationic hydrophobic peptides. *Angew. Chem. Int. Ed.* (2015), *54*, 11735–11739.

50. Izgu, E. C.; Bjorkbom, A.; Kamat, N. P.; Lelyveld, V. S.; Zhang, W.; Jia, T. Z.; Szostak, J. W., *N*-carboxyanhydride-mediated fatty acylation of amino acids and peptides for functionalization of protocell membranes. *J. Am. Chem. Soc.* (2016), *138*, 16669–16676.

51. Lou, J.; Best, M. D. A general approach to enzyme-responsive liposomes. *Chem. Eur. J.* (2020), *26*, 8597–8607.

52. Lyu, Y.; Peng, R.; Liu, H.; Kuai, H.; Mo, L.; Han, D.; Li, J.; Tan, W. Protocells programmed through artificial reaction networks. *Chem. Sci.* (2020), *11*, 631–642.

53. Boyd, M. A.; Kamat, N. P. Designing artificial cells towards a new generation of biosensors. *Trends Biotechnol.* (2021), *39*, 927–939.

54. Schwarz, D. S.; Blower, M. D. The endoplasmic reticulum: structure, function and response to cellular signaling. *Cell Mol Life Sci.* (2016), *1*, 79-94.

55. Bhattarai, K. R.; Riaz, T. A.; Kim, H.-R.; Chae, H.-J. The aftermath of the interplay between the endoplasmic reticulum stress response and redox signaling. *Exp. Mol. Med.* (2021), *53*, 151–167.

56. Krusenstiern, A. N. von; Robson, R. N.; Qian, N.; Qiu, B.; Hu, F.; Reznik, E.; Smith, N.; Zandkarimi, F., Estes, V. M.; Dupont, M.; Hirschhorn, T.; Shchepinov, M. S.; Min, W.; Woerpel, K. A.; Stockwell, B. R. Identification of essential sites of lipid peroxidation in ferroptosis. *Nat. Chem. Biol.* (2023), 1–12.